




Gauge-dependent topology in non-reciprocal hopping systems with pseudo-Hermitian symmetry

Xintong Zhang ¹, Ke Xu¹, Chunmin Liu¹, Xiaoxiao Song¹, Bowen Hou¹, Rui Yu^{2✉}, Hao Zhang ^{1✉}, Dan Li³ & Jing Li ^{1✉}

Energy conservation is not valid in non-Hermitian systems with gain/loss or non-reciprocity, which leads to various extraordinary resonant characteristics. Compared with Hermitian systems, the intersection of non-Hermitian physics and topology generates new phases that have not been observed in condensed-matter systems before. Here, utilizing the designed two-dimensional periodical model with non-reciprocal hopping terms, we show how to obtain both the ellipse-like or hyperbolic-like spectral degeneracy, the topological boundary modes and the bulk-boundary correspondence by the protection of time-reversal symmetry and pseudo-Hermitian symmetry. Notably, the boundary modes and bulk-boundary correspondence can simultaneously appear only for specific selection of the primitive cell, and we explored the analytical solution to verify such gauge-dependent topological behaviors. Our topoelectrical circuit simulation provides a flexible approach to confirm the designed properties and clarify the crucial role of pseudo-Hermiticity on the stability of a practical system. In a broader view, our findings can be compared to other platforms such as meta-surface or photonic crystals, for the purpose on the control of resonant frequency and localization properties.

¹Key Laboratory of Micro and Nano Photonic Structures (MOE), Department of Optical Science and Engineering, Fudan University, Shanghai, China. ²School of Physics and Technology, Wuhan University, Wuhan, China. ³Department of Electronic Engineering, Fudan University, Shanghai, China.
✉email: yurui@whu.edu.cn; zhangh@fudan.edu.cn; lijing@fudan.edu.cn

Non-Hermitian systems which possess gain/loss or non-reciprocal hopping terms, have attracted great attention due to their fantastic resonant characteristics^{1,2}. For example, the spectral degeneracy is always along with the reduction of eigenstates, which is the so-called exceptional point (EP)³⁻⁷, distinctive from the Dirac point or Weyl point in Hermitian systems. The intersection of non-Hermitian physics and topology can also lead to novel phenomenon, such as the non-Hermitian skin effect that all the delocalized eigenstates become localized at the boundary or the corner when the periodical boundary condition (PBC) changes to the open boundary condition (OBC)⁸⁻¹², resulting in the breakdown of bulk-boundary correspondence¹³. These properties, realized in diverse systems such as mechanical metamaterials¹⁴, quantum walk systems¹⁵, photonic systems^{7,16}, acoustic systems¹⁷, and electrical circuits¹⁸⁻²³, have created opportunities to achieve significant enhancement of the sensitivity for sensors²⁴, or perfect absorption of the input wave²⁵.

To investigate the spectral degeneracy characteristic in the higher dimension, recent works have extended the exceptional point to exceptional ring (ER)²⁶⁻³⁰ or exceptional surface (ES)^{31,32}, theoretically. In addition, when combining the non-Hermitian systems with topological behaviors, the topological invariants defined in Hermitian systems cannot predict the existence of the boundary modes any more³³. Several methods have been proposed to solve this issue^{10,33-37}, but the limitation manifests as the particular precondition that point gap or line gap should exist under PBC³⁸.

In this study, we utilized an uncomplicated two-dimensional (2D) non-reciprocal hopping model, and extended the spectral degeneracy characteristic into exceptional elliptical rings and exceptional hyperbolic lines. We show how to design the exceptional rings, the topological boundary modes and the bulk-boundary correspondence, by the protection of time-reversal symmetry and pseudo-Hermitian symmetry. We found that the selection of the primitive cell influences the appearance of boundary modes, which is the so-called gauge-dependent topological behaviors, and can be predicted by the well defined topological invariant successfully even for the condition that no gap exists under PBC. Attentively, the skin effect and the breakdown of bulk-boundary correspondence cannot occur in our model due to the pseudo-Hermitian symmetry³⁸⁻⁴⁰, verified by the transfer-matrix method¹⁰ as well. Furthermore, to extend the theoretical model in a practical system easily, we designed a 2D non-reciprocal hopping topoelectrical circuit lattice, and confirmed the spectral degeneracy characteristic and topological behaviors through circuit simulation, which even can be compared to other platforms such as photonics, acoustics, mechanics and meta-surface.

Results and discussion

Non-reciprocity and spectral degeneracy. Compared with on-site gain/loss systems, systems with non-reciprocal hopping terms provide more freedom on the flexible realization of different types of spectral degeneracy in 2D non-Hermitian systems. For simplicity and without loss of generality, we started with a 2×2 tight-binding model described by $H(\mathbf{k}) = d_0\sigma_0 + d_x\sigma_x + d_y\sigma_y + d_z\sigma_z$ in the momentum space, where $d_0 = \varepsilon_0$, $d_z = 0$, and

$$\begin{aligned} d_x &= t_0 + \sum_{\alpha=x,y} t_{1\alpha} \cos k_\alpha + i \sum_{\alpha=x,y} \gamma_{1\alpha} \sin k_\alpha, \\ d_y &= iy_0 + \sum_{\alpha=x,y} t_{2\alpha} \sin k_\alpha + i \sum_{\alpha=x,y} \gamma_{2\alpha} \cos k_\alpha. \end{aligned} \quad (1)$$

$\sigma_{x,y,z}$ are Pauli matrices for the spin degree of freedom, and σ_0 represents the identity matrix. According to the real-space

Hamiltonian described in Supplementary Note 1, ε_0 represents the on-site energy, $t_{1\alpha/2\alpha}$ represents the reciprocal part of the hopping terms, while $\gamma_0, \gamma_{1\alpha/2\alpha}$ represent the non-reciprocity of intra-cell interaction and inter-cell interaction between the nearest cells, respectively.

The existence of exceptional ring relies on a sufficient condition that $t_{2\alpha} = 0$ and $\gamma_{1\alpha} = 0$, as proved in Supplementary Note 2, thus the resulted Hamiltonian is protected by time-reversal symmetry and pseudo-Hermitian symmetry, as follows,

$$\begin{aligned} \mathcal{T}H^*(\mathbf{k})\mathcal{T}^{-1} &= H(-\mathbf{k}), \quad \mathcal{T}\mathcal{T}^* = \pm 1, \\ \eta H(\mathbf{k})\eta^{-1} &= H^\dagger(\mathbf{k}), \end{aligned} \quad (2)$$

where \mathcal{T} is a unitary operator, and η is a Hermitian invertible operator⁴¹, which is system-specific in the non-Hermitian context (see Supplementary Note 3). These two symmetries restrict that, if $\Psi_+ = (\Psi_A, \Psi_B)^T$ is an eigenvector of the Hamiltonian with energy $\varepsilon_0 + \varepsilon_1$, then $\Psi_- = (\Psi_A, -\Psi_B)^T$ or $(-\Psi_A, \Psi_B)^T$ is an eigenvector with energy $\varepsilon_0 - \varepsilon_1$ ($\varepsilon_1 \in \mathbb{R}$ or $i\mathbb{R}$). Therefore, spectral degeneracy characteristic occur with coalescent eigenvalues $E_\pm = \varepsilon_0$ and coalescent eigenstates $\Psi_\pm = (1, 0)^T$ or $(0, 1)^T$, if and only if

$$(t_{1x} \pm \gamma_{2x}) \cos k_x + (t_{1y} \pm \gamma_{2y}) \cos k_y = -(t_0 \pm \gamma_0). \quad (3)$$

The solutions to Eq. (3) give various spectral degeneracy behaviors, i.e., hyperbolic lines or elliptical rings, relying on whether the coefficients of $\cos k_x$ and $\cos k_y$ have opposite signs. For example, as shown in Fig. 1a, two exceptional rings cross with each other, while as shown in Fig. 1b, a pair of exceptional hyperbolic lines intersect with an exceptional ring.

For the purpose to reveal the interesting physics of spectral degeneracy, we simplified the model by only considering the non-reciprocity of the intra-cell interaction and assumed that $t_{1x} = t_{1y} = t_1$. The resulted Hamiltonian can be written as,

$$H(k_x, k_y) = \begin{pmatrix} \varepsilon_0 & t_0 + t_1 \cos k_x + t_1 \cos k_y + \gamma_0 \\ t_0 + t_1 \cos k_x + t_1 \cos k_y - \gamma_0 & \varepsilon_0 \end{pmatrix}. \quad (4)$$

Without loss of generality, assuming t_0/t_1 and γ_0/t_1 are positive, we classified the parameter space into four phases by the distinct forms of ER, and the detailed range is illustrated in Table 1. As shown in Fig. 1c-f, phase I and phase II both possess a single ER locating at $\cos k_x + \cos k_y = -(t_0 - \gamma_0)/t_1$ with $\Psi_\pm = (1, 0)^T$, but encircle (π, π) and $(0, 0)$ respectively. Phase III and phase IV both possess two ERs, locating at $\cos k_x + \cos k_y = -(t_0 \pm \gamma_0)/t_1$ with $\Psi_\pm = (0, 1)^T$ and $(1, 0)^T$, where the former encircle $(0, 0)$ and (π, π) , while the latter encircle (π, π) and (π, π) .

Gauge-dependent non-Hermitian topology. As we know, the behavior of real systems is often sensitive to the boundary conditions, and the open boundary condition sometimes introduces the localized modes at the boundary or the corner. The intersection of non-Hermitian physics and topology also brings out new phases. For simplicity, we imposed OBC along x direction and PBC along y direction in the lattice model, and the system can be understood as the effective one-dimensional chain parametrized by the transverse momentum k_y (see Supplementary Note 4.1). Two kinds of OBC are proposed for comparison. OBC₁ requires that the hopping terms between the first and the last cells are removed from the periodic lattice, as shown in Fig. 2a. For OBC₂ shown in Fig. 2b, the difference from OBC₁ is the selection of the primitive cell, which can be regarded as the gauge transformation that $H'(k_x, k_y) = S^{-1}H(k_x, k_y)S$ with $S = \text{diag}(e^{ik_x}, 1)$, which possesses the same symmetry and spectrum as $H(k_x, k_y)$

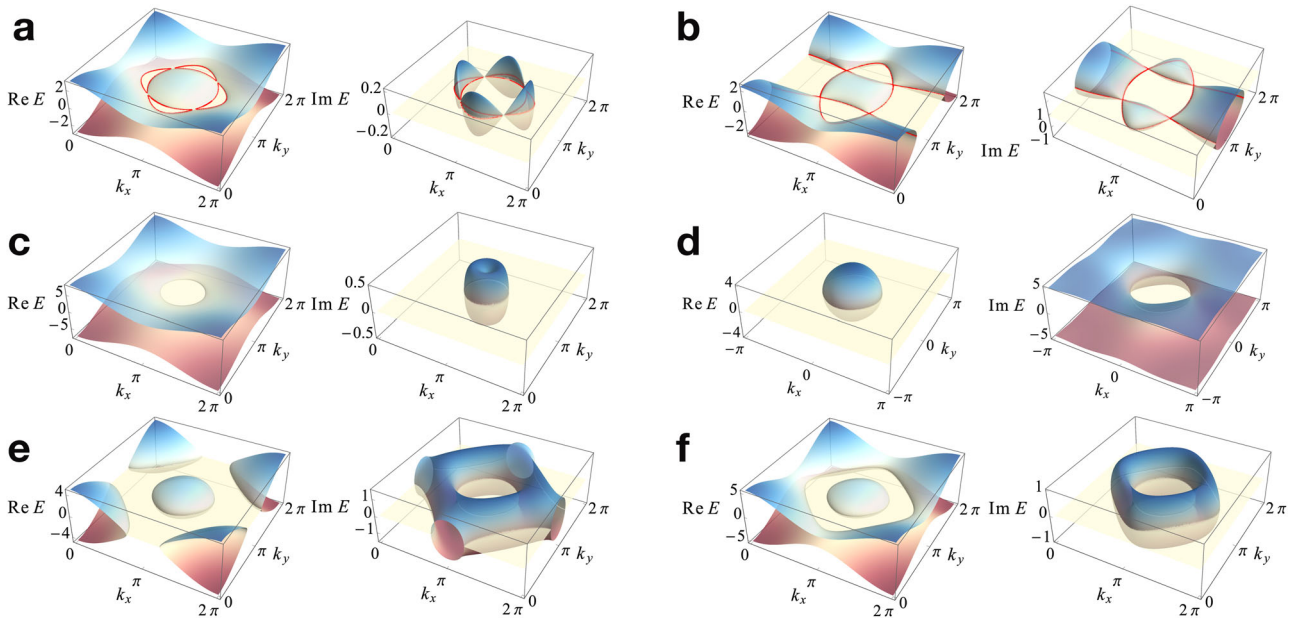


Fig. 1 The real and imaginary parts of the energy spectra under periodical boundary condition. The blue and purple parts represent the eigenvalues E_+ and E_- respectively, where $E_{\pm} = \epsilon_0 \pm \sqrt{d_x^2 + d_y^2}$, and the red lines denote the spectral degeneracy that $E_+ = E_- = \epsilon_0$. For simplicity and without loss of generality, the on-site energy ϵ_0 is set as zero, and the hopping parameters are set as $t_{1x} = t_{1y} = t_1$. **a, b** The energy spectra defined by $E_{\pm} = \pm \sqrt{(t_0 + t_1 \cos k_x + t_1 \cos k_y)^2 - (\gamma_0 + \gamma_{2x} \cos k_x)^2}$ with hopping parameters $t_0/t_1 = 1$, $\gamma_0/t_1 = 0.2$, $\gamma_{2x}/t_1 = 0.4$ in **(a)**, and $t_0/t_1 = 1$, $\gamma_0/t_1 = 0.6$, $\gamma_{2x}/t_1 = 1.2$ in **(b)**, which can exhibit exceptional rings and hyperbolic lines respectively. **c-f** The energy spectra defined by $E_{\pm} = \pm \sqrt{(t_0 + t_1 \cos k_x + t_1 \cos k_y)^2 - \gamma_0^2}$. The parameter space is classified into phase I-IV by the distinct forms of the exceptional rings. **c** Phase I with $t_0/t_1 = 1.85$, $\gamma_0/t_1 = 0.25$. **d** Phase II with $t_0/t_1 = 1.2$, $\gamma_0/t_1 = 2.5$. **e** Phase III with $t_0/t_1 = 0.5$, $\gamma_0/t_1 = 0.75$. **f** Phase IV with $t_0/t_1 = 0.75$, $\gamma_0/t_1 = 0.5$.

Table 1 Illustration to the phase diagram of the tight-binding model. The parameter space (t_0, t_1, γ_0) is classified into phase I-IV according to the distinct locations and centers of the exceptional ring (ER) in the momentum space (k_x, k_y) . Phase I and phase II both possess a single exceptional ring, but encircle (π, π) and $(0, 0)$ respectively. Phase III and phase IV both possess two exceptional rings, where the former encircle (π, π) and $(0, 0)$, while the latter encircle (π, π) and (π, π) .

Phase	Parameters	Location of ER	Center of ER
I	$(t_0 + \gamma_0)/t_1 \in (2, \infty) \& (t_0 - \gamma_0)/t_1 \in (0, 2)$	$\cos k_x + \cos k_y = -(t_0 - \gamma_0)/t_1$	(π, π)
II	$(t_0 + \gamma_0)/t_1 \in (2, \infty) \& (t_0 - \gamma_0)/t_1 \in (-2, 0)$	$\cos k_x + \cos k_y = -(t_0 - \gamma_0)/t_1$	$(0, 0)$
III	$(t_0 + \gamma_0)/t_1 \in (0, 2) \& (t_0 - \gamma_0)/t_1 \in (-2, 0)$	$\cos k_x + \cos k_y = -(t_0 + \gamma_0)/t_1$ $\cos k_x + \cos k_y = -(t_0 - \gamma_0)/t_1$	(π, π) $(0, 0)$
IV	$(t_0 + \gamma_0)/t_1 \in (0, 2) \& (t_0 - \gamma_0)/t_1 \in (0, 2)$	$\cos k_x + \cos k_y = -(t_0 + \gamma_0)/t_1$ $\cos k_x + \cos k_y = -(t_0 - \gamma_0)/t_1$	(π, π) (π, π)

under PBC, but leads to the distinct difference in topological behaviors.

The numerical results for OBC₁ and OBC₂ spectra are shown in Fig. S3 in Supplementary Note 4.1 and Fig. 3a, d respectively, which reveal that the former is trivial, while the latter generates topological boundary modes at the on-site energy ϵ_0 , which is the so-called topological non-triviality. For example, using the parameters belonging to phase I, the OBC₂ spectrum is shown in Fig. 3a, where the bulk modes are denoted by gray lines, and the topological boundary modes denoted by orange lines can exist for any $k_y \in (0, 2\pi)$. Correspondingly, the normalized amplitude of the localized wave function is shown in Fig. 3b.

To investigate the underlying mechanism of the existence or non-existence of topological boundary modes, we followed a convenient criterion applied for one-dimensional systems³⁵. Generally, by polynomial factorization and rescaling the overall constants to unity without changing the topology, the

Hamiltonian can be rewritten as,

$$H(z) = \begin{pmatrix} 0 & a(z) \\ b(z) & 0 \end{pmatrix} = \begin{pmatrix} 0 & z^{-q_a} \prod_i^{p_a} (z - a_i) \\ z^{-q_b} \prod_i^{p_b} (z - b_i) & 0 \end{pmatrix}, \quad (5)$$

where the on-site energy is set to zero, and $z = e^{ik_x}$, $k_x \in \mathbb{C}$. q_a, q_b count the numbers of poles locating at $z = 0$, and $\{a_1, \dots, a_{p_a}\}, \{b_1, \dots, b_{p_b}\}$ are the complex roots of $a(z) = 0$, $b(z) = 0$ respectively. The topological boundary modes exist if and only if $\exists R \in \mathbb{R}_+, W_a(R)W_b(R) < 0$ ³⁵, where the winding number $W_{g(=a/b)}(R)$ is defined as $\frac{1}{2\pi i} \oint_{|z|=R} d(\log g(=a/b)(z))$, which counts the number of zeros minus the number of poles encircled by the contour $|z| = R$. Through the calculation on winding numbers (see Supplementary Note 4.2), the criterion of the topological non-triviality can be reformulated as the fundamental

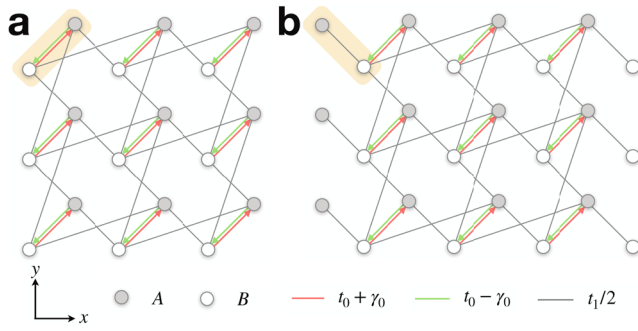


Fig. 2 Schematic views of the two-dimensional tight-binding model under open boundary condition (OBC) along x direction. The gray and white circles represent the two sites A and B , and the yellow blocks indicate the selection of the primitive cell. The non-reciprocal hopping terms with parameters $t_0 \pm \gamma_0$ are denoted by orange and green lines with arrows, while the reciprocal hopping terms with parameter $t_1/2$ are denoted by gray lines. **a** Lattice model under OBC_1 . **b** Lattice model under OBC_2 .

principles that,

- (i) for OBC_1 , $\max\{|a_1|, |a_2|\} < \min\{|b_1|, |b_2|\}$ or $\max\{|b_1|, |b_2|\} < \min\{|a_1|, |a_2|\}$,
- (ii) for OBC_2 , $\min\{|b_1|, |b_2|\} < \max\{|a_1|, |a_2|\}$,

(6)

where $\{a_1, a_2, b_1, b_2\}$ are the solutions to $\text{Det } H(z) = 0$ for both OBC_1 and OBC_2 . For example, for the case belonging to phase I, $\{|a_1|, |a_2|, |b_1|, |b_2|\}$ curves are shown in Fig. 3c, which demonstrates that, criterion (i) is impossible to be satisfied, verifying the non-existence of topological boundary modes for OBC_1 . However, criterion (ii) can be satisfied for OBC_2 , where the colored regions satisfy the condition that $W_a(R)$ and $W_b(R)$ have opposite signs, confirming the existence of topological boundary modes. The winding number $W(R)$ is defined as $[W_a(R) - W_b(R)]/2$, and the zero value of this topological invariant represents the non-existence of topological boundary modes. The case for phase IV is shown in Fig. 3d–f, where the topological boundary modes can appear only when $\cos k_y < 1 - (t_0 + \gamma_0)/t_1$, which also can be verified by the criterion(ii) in Eq. (6).

We also explored the distribution properties of the topological eigenstates, in accordance with the biorthogonal bulk-boundary correspondence theory^{13,42–44} (see Supplementary Note 5). For example, as shown in Fig. 3b, when $|a_2| < 1, |b_2| < 1$, two topological eigenstates are localized at both ends along x direction with penetration length $-1/\ln |b_2|$ ($n=1$, on A sites) and $-1/\ln |a_2|$ ($n=N$, on B sites). In addition, when $|a_2| < 1, |b_2| = 1$, two topological modes are identical to each other and both localized at $n=N$ along x direction, on B sites, with penetration length $-1/\ln |a_2|$. Furthermore, the relevant biorthogonal polarization was calculated to predict the appearance of topological modes, consistent with the results derived from winding numbers.

Both OBC_1 and OBC_2 systems exhibit the conventional bulk-boundary correspondence and non-existence of skin effect, where the bulk modes under OBC are consistent with those under PBC. It should be noted that, symmetry plays a significant role in our non-reciprocal hopping model. Restricted by the pseudo-Hermiticity, the bulk Hamiltonian is generally insensitive to the boundary conditions, because the wave numbers are real even in the generalized Brillouin zone³⁸, thus the bulk modes are delocalized. To further investigate the connection between the non-existence of the non-Hermitian skin effect and the restoration of the bulk-boundary correspondence, we followed the transfer-matrix method¹⁰, and found that $|\det T| = 1$ for our model (see Supplementary Note 6).

Topolectrical circuit lattice. To clarify the previous results and explore the crucial role of pseudo-Hermitian symmetry in a practical system, we designed a 2D topolectrical circuit to map the tight-binding model. As shown in Fig. 4a, following the method described by Yu et al.²⁰, the A/B site in the tight-binding model corresponds to the A/B junction in the circuit lattice, and the reciprocal hopping term between sites corresponds to the capacitor which connects the junctions, while the non-reciprocal interaction is realized by the operational amplifier which operates as a voltage follower. Furthermore, the 2D circuit lattice contains 80 sub-circuits, and each sub-circuit contains 20 unit cells arranged along y direction. The connection between the two sub-circuits is illustrated in Fig. 4b. Followed by the Kirchhoff's Laws described in Methods, the effective Hamiltonian H_e for the circuit lattice is given by

$$H_e(k_x, k_y) = \begin{pmatrix} C_A + C_y + C_m + 4C_t & -2C_t(\cos k_x + \cos k_y) - C_m - C_y \\ -2C_t(\cos k_x + \cos k_y) - C_m & C_B + C_m + 4C_t \end{pmatrix}, \quad (7)$$

where $C_m = -(t_0 - \gamma_0)$, $C_t = -t_1/2$ and $C_y = -2\gamma_0$ and $C_A + C_y = C_B$, by comparing with the model Hamiltonian. The resonant frequency ω corresponds to the eigenvalue E with the relation of $\omega = 1/\sqrt{EL}$, where L represents the inductor value. Therefore, various phases can be realized in topolectrical circuits through tuning the values of capacitors. The voltage signals $V(\mathbf{r}, t)$ of the $2N^2$ ($N=40$) junctions can be extracted after the transient analysis of the circuit simulation, and then through Fourier transformation, the amplitude of eigenstates $V(\mathbf{f})$ in the frequency domain can be calculated.

We carried out the simulation to realize the frequency response of phase I and phase IV for both PBC and OBC_2 , because $(t_0 - \gamma_0)/t_1 > 0$ should be satisfied to avoid negative values of capacitors. As shown in Fig. 5a, for phase I under PBC, the simulated frequency response colored by gray is consistent with the ideal spectra, and the single ER which locates at $\cos k_x + \cos k_y = -C_m/(2C_t) = -1.6$, is shown in Fig. 5b. The results of the OBC system are shown in Fig. 5c, d, which reveals that, when stimulated by the on-site frequency, both of the bulk modes and the topological boundary modes exist, and the combined modes are localized at the left side of the circuit lattice, if the source is only placed at the left boundary to avoid signal divergence. Similarly, as shown in Fig. 5e–h, the ERs of phase IV locate at $\cos k_x + \cos k_y = -C_m/(2C_t) = -0.5$ and $\cos k_x + \cos k_y = -(C_m + C_y)/(2C_t) = -1$, and the combined modes stimulated by the on-site frequency are localized at the left side as well. Owing to the pseudo-Hermitian symmetry, in spite of the negative imaginary part of the frequency, the system is still stable in time domain, which can be used as reference for further experimental maneuverability. As mentioned above, the eigenstates $\Psi_+ = (V_A(\mathbf{k}), V_B(\mathbf{k}))^T$ is always paired with $\Psi_- = (-V_A(\mathbf{k}), V_B(\mathbf{k}))^T$ or $(V_A(\mathbf{k}), -V_B(\mathbf{k}))^T$ under PBC, thus the voltage signal is approximately equal to $|\Psi_+|e^{-\text{Im}[\omega]t}e^{i\text{Re}[\omega]t}$. Therefore, the amplitude of the voltage cannot diverge seriously within several time periods.

Conclusions

In conclusion, we have proposed the general form of the two-dimensional non-reciprocal hopping model protected by time-reversal symmetry and pseudo-Hermitian symmetry, which exhibits exceptional elliptical rings or exceptional hyperbolic lines under PBC. The simplified form is mainly discussed, and the parameters space is classified into phases I–IV, according to the distinct forms of exceptional rings. Through the suitable selection of the primitive cell, the topological boundary modes can appear for all four phases, which is verified by the non-zero winding

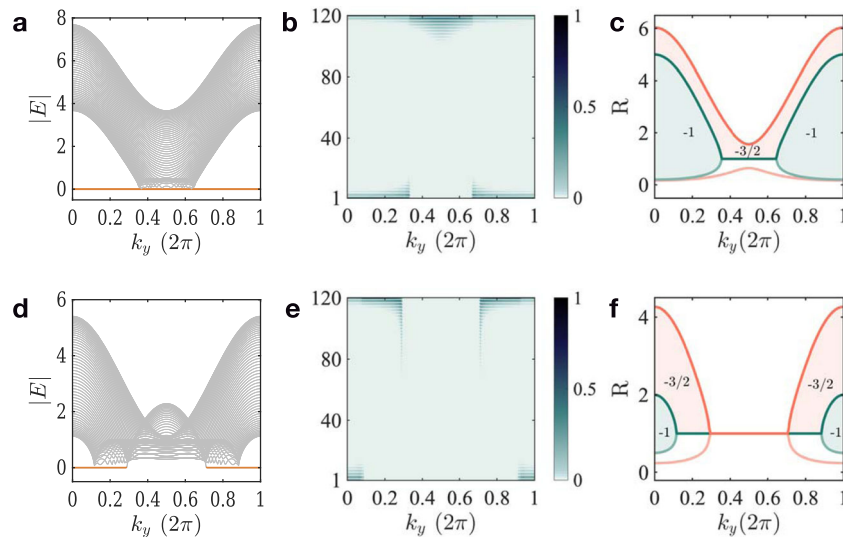


Fig. 3 Topological behaviors of the effective one-dimensional tight-binding model under open boundary condition. **a–c** Show the results for phase I with hopping parameters $t_0/t_1 = 1.85$, $\gamma_0/t_1 = 0.25$, and **(d–f)** show the results for phase IV with $t_0/t_1 = 0.75$, $\gamma_0/t_1 = 0.5$. **a, d** The absolute values of the energy spectra $|E|$ for $k_y \in (0, 2\pi)$ with on-site energy $\epsilon_0 = 0$, where gray and orange lines denote bulk modes and topological boundary modes, respectively. **b, e** The absolute values of the normalized amplitude of the localized topological boundary modes with $N = 60$ unit cells ($2N$ sites) along x direction. **c, f** $|a_1|$, $|a_2|$, $|b_1|$, $|b_2|$ curves are colored by red, light red, dark green and light green, respectively, where $a_{1,2} = -[(t_0 + \gamma_0)/t_1 + \cos k_y] \mp \sqrt{[(t_0 + \gamma_0)/t_1 + \cos k_y]^2 - 1}$ and $b_{1,2} = -[(t_0 - \gamma_0)/t_1 + \cos k_y] \mp \sqrt{[(t_0 - \gamma_0)/t_1 + \cos k_y]^2 - 1}$, and the colored regions marked by the non-zero winding numbers $W(R)$ satisfy the condition of topological boundary modes.

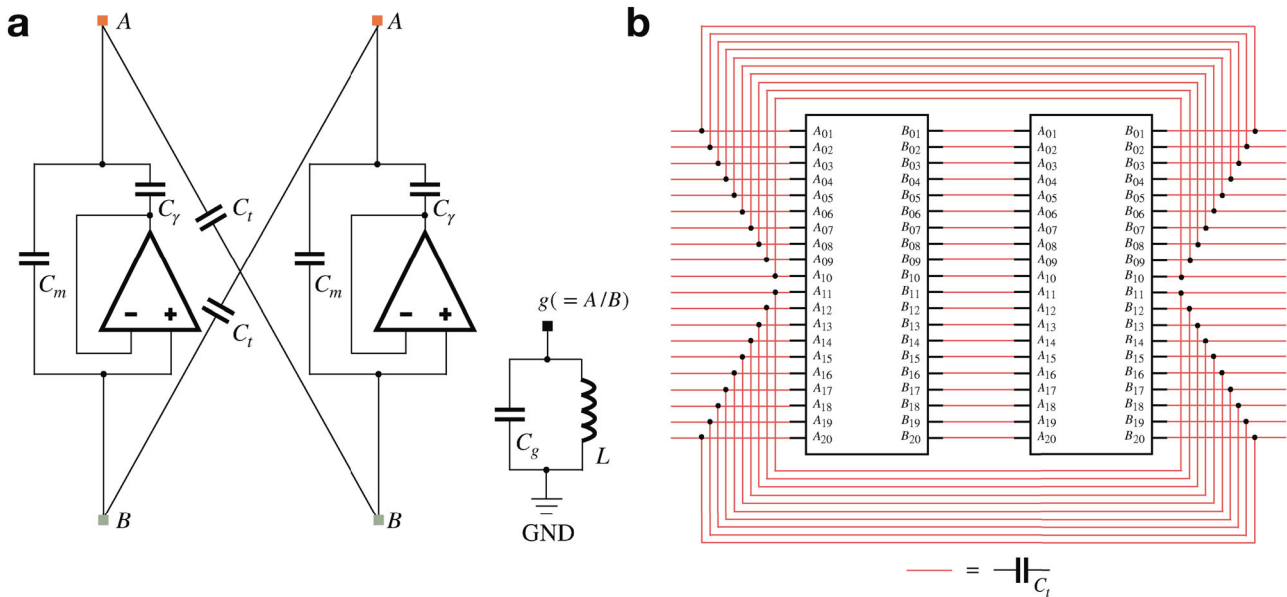


Fig. 4 Schematic illustration of the two-dimensional topoelectrical circuit. **a** Two unit cells in the circuit lattice. The reciprocal hopping terms are realized by capacitors C_m , and the non-reciprocal hopping terms are realized by the operational amplifiers and capacitors C_γ , where current flow can exist between A sites and the output of the amplifier, but cannot exist between B sites and the input of the amplifier. The LC-circuits which connect the A/B sites and the ground provide the on-site frequency response. **b** The 40×40 lattice contains 80 sub-circuits, and each sub-circuit contains 20 unit cells, arranged along y direction. The schematic view shows the connection between two sub-circuits along x direction, where A_n, B_n denote the sites of the n th unit cell inside the sub-circuit, and the connection between the unit cells is the same as **(a)**.

numbers, and the penetration lengths of the topological boundary modes are analyzed through the biorthogonal bulk-boundary correspondence method. In addition, in the presence of pseudo-Hermitian symmetry, our non-Hermitian model behaves like the Hermitian system under OBC, where the bulk-boundary correspondence exists and the non-Hermitian skin effect vanishes, verified by $|\det T| = 1$. Finally, we designed the proposed phase I

and phase IV in the topoelectrical circuits, and the simulation results not only correspond to those in the model, but also demonstrate the crucial role of pseudo-Hermitian symmetry in a practical system. In a broader view, our findings can be compared to other platforms such as photonics, acoustics, mechanics or meta-surface, for the purpose on the control of frequency response and localization properties.

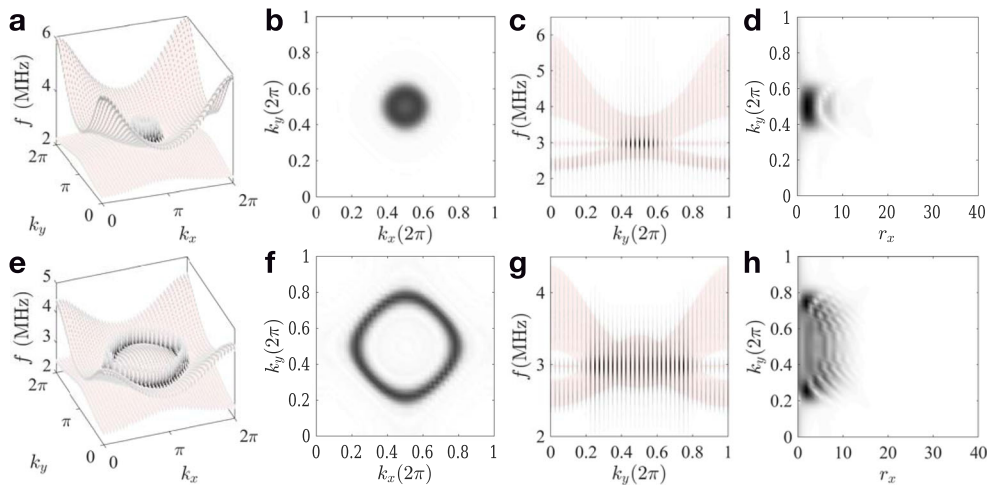


Fig. 5 Simulation results of the topoelectrical circuit. **a–d** Show the results for phase I with electronic components $L = 5.6 \mu\text{H}$, $C_A = 100 \text{ pF}$, $C_B = 150 \text{ pF}$, $C_m = 160 \text{ pF}$, $C_t = C_r = 50 \text{ pF}$, and **(e–h)** show the results for phase IV with components $L = 5.6 \mu\text{H}$, $C_A = 210 \text{ pF}$, $C_B = 260 \text{ pF}$, $C_m = C_t = C_r = 50 \text{ pF}$. **a, e** Frequency response of the topoelectrical circuit lattice under periodical boundary condition, where the ideal model results and simulation results are colored by light red and gray respectively. **b, f** Exceptional rings stimulated by the on-site frequency $f_0 = 1/(2\pi\sqrt{(C_B + C_m + 4C_t)L})$. **c, g** Frequency response of the topoelectrical circuit under open boundary condition. **d, h** The amplitude of the localized topological boundary modes stimulated by the on-site frequency.

Methods

Derivation of the effective Hamiltonian for circuit lattice. As shown in Fig. 4a, the non-reciprocal interaction is realized by the operational amplifier which operates as a voltage follower. Ideally, when working at the linear region, the operational amplifier can amplify the difference of voltage between the two inputs, and the output voltage is given by $V_{out} = \beta(V_+ - V_-)$, where β is the open-loop gain, and V_{\pm} is the voltage of the non-inverting/inverting input. Therefore, if the inverting input is connected to the output and the non-inverting input is connected to junction B, which means $V_- = V_{out}$, $V_+ = V_B$, thus $V_{out} = \frac{\beta}{\beta+1}V_B$. Since β is generally large enough for amplifiers, the voltage of the output of amplifier equals to V_B and no current flows through the two inputs.

Based on Kirchhoff's Law that the sum of current into a junction equals the sum of current out of the junction, the currents through junction A and B can be written as

$$\begin{aligned} I_A &= i\omega C_A(0 - V_A) + \frac{1}{i\omega L}(0 - V_A) + i\omega C_m(V_B - V_A) + i\omega C_t(V_B e^{ik_x} - V_A) + i\omega C_r(V_B e^{-ik_x} - V_A) \\ &\quad + i\omega C_l(V_B e^{ik_y} - V_A) + i\omega C_l(V_B e^{-ik_y} - V_A) + i\omega C_r(V_B - V_A) = 0, \\ I_B &= i\omega C_B(0 - V_B) + \frac{1}{i\omega L}(0 - V_B) + i\omega C_m(V_A - V_B) + i\omega C_t(V_A e^{ik_x} - V_B) + i\omega C_r(V_A e^{-ik_x} - V_B) \\ &\quad + i\omega C_l(V_A e^{ik_y} - V_B) + i\omega C_l(V_A e^{-ik_y} - V_B) = 0. \end{aligned} \quad (8)$$

Rewriting the equation above into a matrix form, the effective Schrödinger's equation for the periodic circuit lattice is given by,

$$H_c \begin{pmatrix} V_A \\ V_B \end{pmatrix} = \frac{1}{\omega^2 L} \begin{pmatrix} V_A \\ V_B \end{pmatrix}, \quad (9)$$

where the voltage V_A/V_B at A/B junctions corresponds to the wave function Ψ_A/Ψ_B , and the resonant frequency ω corresponds to the eigenvalue E with the relation of $\omega = 1/\sqrt{EL}$. The effective Hamiltonian H_c for the circuit lattice is given by Eq. (7).

Simulation details. Transient analysis and Fourier transformation were carried out to simulate the frequency response of the designed topoelectrical circuit. First, the amplifiers, capacitors and inductors were selected as ideal elements, and the values of the components are chosen to limit that the resonant frequency ranges from 10^5 to 10^6 Hz, for further practical consideration. Secondly, the source of the lattice is set as pulse-excitation with $6 \mu\text{s}$ width, $0.1 \mu\text{s}$ rising edge and $0.2 \mu\text{s}$ falling edge. For OBC, the source was placed at the left of the circuit lattice, while for PBC, the source can be placed at any position of the lattice. Third, to satisfy the Nyquist sampling theorem, the total time of the transient analysis is set as $12 \mu\text{s}$ for both PBC and OBC with time step 10 ns , and the frequency step was set as 10 kHz when operating the Fourier transformation.

Data availability

The data that support the plots within this paper are available from the corresponding author on reasonable request.

Code availability

The computer codes used to generate the data presented in the manuscript are available from the corresponding author on reasonable request.

Received: 13 December 2020; Accepted: 29 June 2021;

Published online: 20 July 2021

References

- Bergholtz, E. J., Budich, J. C. & Kunst, F. K. Exceptional topology of non-hermitian systems. *Rev. Mod. Phys.* **93**, 015005 (2021).
- Ashida, Y., Gong, Z. & Ueda, M. Non-hermitian physics. *Adv. Phys.* **69**, 249–435 (2020).
- Heiss, W. D. The physics of exceptional points. *J. Phys. A: Math. Theor.* **45**, 444016 (2012).
- Leykam, D., Bliokh, K. Y., Huang, C., Chong, Y. D. & Nori, F. Edge modes, degeneracies, and topological numbers in non-hermitian systems. *Phys. Rev. Lett.* **118**, 040401 (2017).
- Zhang, H. et al. Breaking anti-pt symmetry by spinning a resonator. *Nano Lett.* **20**, 7594–7599 (2020).
- Martinez Alvarez, V. M., Barrios Vargas, J. E. & Foa Torres, L. E. F. Non-hermitian robust edge states in one dimension: Anomalous localization and eigenspace condensation at exceptional points. *Phys. Rev. B* **97**, 121401 (2018).
- Song, W. et al. Breakup and recovery of topological zero modes in finite non-hermitian optical lattices. *Phys. Rev. Lett.* **123**, 165701 (2019).
- Liu, T. et al. Second-order topological phases in non-hermitian systems. *Phys. Rev. Lett.* **122**, 076801 (2019).
- Lee, C. H., Li, L. & Gong, J. Hybrid higher-order skin-topological modes in nonreciprocal systems. *Phys. Rev. Lett.* **123**, 016805 (2019).
- Kunst, F. K. & Dwivedi, V. Non-hermitian systems and topology: A transfer-matrix perspective. *Phys. Rev. B* **99**, 245116 (2019).
- Song, F., Yao, S. & Wang, Z. Non-hermitian skin effect and chiral damping in open quantum systems. *Phys. Rev. Lett.* **123**, 170401 (2019).
- Yoshida, T., Mizoguchi, T. & Hatsugai, Y. Mirror skin effect and its electric circuit simulation. *Phys. Rev. Res.* **2**, 022062 (2020).
- Edvardsson, E., Kunst, F. K., Yoshida, T. & Bergholtz, E. J. Phase transitions and generalized biorthogonal polarization in non-hermitian systems. *Phys. Rev. Res.* **2**, 043046 (2020).
- Ghatak, A., Brandenbourger, M., van Wezel, J. & Coullais, C. Observation of non-hermitian topology and its bulk-edge correspondence in an active mechanical metamaterial. *Proc. Natl Acad. Sci. USA.* **117**, 29561–29568 (2020).
- Xiao, L. et al. Non-hermitian bulk-boundary correspondence in quantum dynamics. *Nat. Phys.* **16**, 761–766 (2020).

16. Wang, H. et al. Exceptional concentric rings in a non-hermitian bilayer photonic system. *Phys. Rev. B* **100**, 165134 (2019).
17. Zhu, W. et al. Simultaneous observation of a topological edge state and exceptional point in an open and non-hermitian acoustic system. *Phys. Rev. Lett.* **121**, 124501 (2018).
18. Luo, K., Yu, R. and Weng, H. Topological nodal states in circuit lattice. *Research*. 2018, 6793752 (2018) <https://spj.science.org/journals/research/2018/6793752/>.
19. Lee, C. H. et al. Topoelectrical circuits. *Commun. Phys.* **1**, 39 (2018).
20. Yu, R., Zhao, Y. X. and Schnyder, A. P. 4D spinless topological insulator in a periodic electric circuit. *Natl. Sci. Rev.* **04** 2020. nwa065.
21. Hofmann, T. et al. Reciprocal skin effect and its realization in a topoelectrical circuit. *Phys. Rev. Res.* **2**, 023265 (2020).
22. Rafi-Ul-Islam, S. M., Bin Sui, Z. & Jalil, M. B. A. Topoelectrical circuit realization of a weyl semimetal heterojunction. *Commun. Phys.* **3**, 72 (2020).
23. Zhang, W. et al. Experimental observation of higher-order topological anderson insulators. *Phys. Rev. Lett.* **126**, 146802 (2021).
24. Djorwe, P., Pennec, Y. & Djafari-Rouhani, B. Exceptional point enhances sensitivity of optomechanical mass sensors. *Phys. Rev. Appl.* **12**, 024002 (2019).
25. Sweeney, W. R., Hsu, C. W., Rotter, S. & Stone, A. D. Perfectly absorbing exceptional points and chiral absorbers. *Phys. Rev. Lett.* **122**, 093901 (2019).
26. Budich, J. C., Carlström, J., Kunst, F. K. & Bergholtz, E. J. Symmetry-protected nodal phases in non-hermitian systems. *Phys. Rev. B* **99**, 041406 (2019).
27. Wang, H., Ruan, J. & Zhang, H. Non-hermitian nodal-line semimetals with an anomalous bulk-boundary correspondence. *Phys. Rev. B* **99**, 075130 (2019).
28. Cerjan, A. et al. Experimental realization of a weyl exceptional ring. *Nat. Photonics* **13**, 623–628 (2019).
29. Yoshida, T., Peters, R., Kawakami, N. & Hatsugai, Y. Symmetry-protected exceptional rings in two-dimensional correlated systems with chiral symmetry. *Phys. Rev. B* **99**, 121101 (2019).
30. Yang, Z. & Hu, J. Non-hermitian hopf-link exceptional line semimetals. *Phys. Rev. B* **99**, 081102 (2019).
31. Okugawa, R. & Yokoyama, T. Topological exceptional surfaces in non-hermitian systems with parity-time and parity-particle-hole symmetries. *Phys. Rev. B* **99**, 041202 (2019).
32. Zhong, Q. et al. Sensing with exceptional surfaces in order to combine sensitivity with robustness. *Phys. Rev. Lett.* **122**, 153902 (2019).
33. Yao, S. & Wang, Z. Edge states and topological invariants of non-hermitian systems. *Phys. Rev. Lett.* **121**, 086803 (2018).
34. Yokomizo, K. & Murakami, S. Non-bloch band theory of non-hermitian systems. *Phys. Rev. Lett.* **123**, 066404 (2019).
35. Lee, C. H. & Thomaie, R. Anatomy of skin modes and topology in non-hermitian systems. *Phys. Rev. B* **99**, 201103 (2019).
36. Okuma, N., Kawabata, K., Shiozaki, K. & Sato, M. Topological origin of non-hermitian skin effects. *Phys. Rev. Lett.* **124**, 086801 (2020).
37. Ghatak, A. & Das, T. New topological invariants in non-hermitian systems. *J. Phys.: Condens. Matter* **31**, 263001 (2019).
38. Kawabata, K., Shiozaki, K., Ueda, M. & Sato, M. Symmetry and topology in non-hermitian physics. *Phys. Rev. X* **9**, 041015 (2019).
39. Kawabata, K., Higashikawa, S., Gong, Z., Ashida, Y. & Ueda, M. Topological unification of time-reversal and particle-hole symmetries in non-hermitian physics. *Nat. Commun.* **10**, 297 (2019).
40. Kawabata, K., Bessho, T. & Sato, M. Classification of exceptional points and non-hermitian topological semimetals. *Phys. Rev. Lett.* **123**, 066405 (2019).
41. Mostafazadeh, A. & Batal, A. Physical aspects of pseudo-hermitian and PT-symmetric quantum mechanics. *J. Phys. A: Math. Gen.* **37**, 11645–11679 (2004).
42. Brody, D. C. Biorthogonal quantum mechanics. *J. Phys. A: Math. Theor.* **47**, 035305 (2013).
43. Kunst, F. K., Trescher, M. & Bergholtz, E. J. Anatomy of topological surface states: exact solutions from destructive interference on frustrated lattices. *Phys. Rev. B* **96**, 085443 (2017).
44. Kunst, F. K., Edvardsson, E., Budich, J. C. & Bergholtz, E. J. Biorthogonal bulk-boundary correspondence in non-hermitian systems. *Phys. Rev. Lett.* **121**, 026808 (2018).

Acknowledgements

We thank for the support from the National Key Research and Development Program of China (Grant Nos. 2017YFA0303402, 2017YFA0304700), the National Natural Science Foundation of China (Grant Nos. 60578047, 11374063, 11874048, 11674077), the Natural Science Foundation of Shanghai (Grant Nos. 17ZR1402200, 13ZR1402600, 18ZR1435700), and the GRF of Hong Kong (Grant No. HKU173057/17P). We thank Kaifa Luo and Yi Jiang for fruitful discussion.

Author contributions

R.Y., H.Z. and J.L. planned the project. X.Z. performed the numerical and analytical calculations, and carried out the circuit simulation. K.X. helped to analyze the topological behaviors. C.L., X.S., B.H. helped to improve the design of models. D.L. helped to analyze the validity of topoelectrical circuits. All authors participated in the discussion on the results, and have read and agreed the published version of the manuscript.

Competing interests

The authors declare no competing interests.

Additional information


Supplementary information The online version contains supplementary material available at <https://doi.org/10.1038/s42005-021-00668-3>.

Correspondence and requests for materials should be addressed to R.Y., H.Z. or J.L.

Peer review information *Communications Physics* thanks the anonymous reviewers for their contribution to the peer review of this work. Peer reviewer reports are available.

Reprints and permission information is available at <http://www.nature.com/reprints>

Publisher's note Springer Nature remains neutral with regard to jurisdictional claims in published maps and institutional affiliations.

 **Open Access** This article is licensed under a Creative Commons Attribution 4.0 International License, which permits use, sharing, adaptation, distribution and reproduction in any medium or format, as long as you give appropriate credit to the original author(s) and the source, provide a link to the Creative Commons license, and indicate if changes were made. The images or other third party material in this article are included in the article's Creative Commons license, unless indicated otherwise in a credit line to the material. If material is not included in the article's Creative Commons license and your intended use is not permitted by statutory regulation or exceeds the permitted use, you will need to obtain permission directly from the copyright holder. To view a copy of this license, visit <http://creativecommons.org/licenses/by/4.0/>.

© The Author(s) 2021